POLITECNICO DI TORINO
Repository ISTITUZIONALE

Fast Efficiency Mapping Procedure for PMSM Accounting for the PWM Supply Impact

Original
Fast Efficiency Mapping Procedure for PMSM Accounting for the PWM Supply Impact / Ragazzo, P., Dilevrano, G., Bojoi, A., Ferrari, S., Pellegrino, G.. - ELETTRONICO. - (2024), pp. 1-6. (2024 IEEE International Conference on Industrial Technology (ICIT) Bristol (UK) 25-27 March 2024) [10.1109/icit58233.2024.10540816].

Availability:
This version is available at: 11583/2989363 since: 2024-06-06T20:06:40Z

Publisher:
IEEE

Published
DOI:10.1109/icit58233.2024.10540816

Terms of use:

This article is made available under terms and conditions as specified in the corresponding bibliographic description in the repository

Publisher copyright
IEEE postprint/Author's Accepted Manuscript

©2024 IEEE. Personal use of this material is permitted. Permission from IEEE must be obtained for all other uses, in any current or future media, including reprinting/republishing this material for advertising or promotional purposes, creating new collecting works, for resale or lists, or reuse of any copyrighted component of this work in other works.

(Article begins on next page)

12 August 2026

Fast efficiency mapping procedure for PMSM accounting for the PWM supply impact

Paolo Ragazzo
Dipartimento Energia Galileo Ferraris
Politecnico di Torino
Turin, Italy
paolo.ragazzo@polito.it

Gaetano Dilevrano
Dipartimento Energia Galileo Ferraris
Politecnico di Torino
Turin, Italy
gaetano.dilevrano@polito.it

Andrei Bojoi
Dipartimento Energia Galileo Ferraris
Politecnico di Torino
Turin, Italy
andrei.bojoi@polito.it

Simone Ferrari
Dipartimento Energia Galileo Ferraris
Politecnico di Torino
Turin, Italy
simone.ferrari@polito.it

Gianmario Pellegrino
Dipartimento Energia Galileo Ferraris
Politecnico di Torino
Turin, Italy
gianmario.pellegrino@polito.it

***Abstract*—This paper introduces a rapid method for computing efficiency maps of PMSMs, taking into consideration the impact of PWM supply. Notably, the efficiency map derived from an ideal sinusoidal supply can significantly deviate from the actual map under inverter supply conditions. However, accommodating the PWM supply effect in the efficiency map computation can be intricate and time-consuming. This manuscript presents a simplified technique to incorporate the PWM impact on the efficiency map by quickly estimating the copper, iron, and magnet loss in a limited grid of operational points across the torque-speed domain. From these points, adjustment factors are determined and subsequently applied to the initial sinusoidal efficiency map. The loss computation is entirely based on simple static FEA with dedicated add-ons to contemplate complex and impactful phenomena, such as the eddy current reaction field. Last, the process is showcased with a V-shaped PMSM for traction application, resembling the one mounted on the rear-axle of the Tesla Model 3.**

***Index Terms*—permanent magnet synchronous machines, efficiency map, static simulation**

I. Introduction

A. Background

In the automotive industry, most traction systems rely on permanent magnet synchronous machines (PMSMs) that are driven by pulse-width modulated (PWM) inverters, as discussed in references [1]. However, the PWM introduces high-frequency harmonics into the motor operation, which adds up to other machine harmonics at lower frequencies. Each of these harmonics contributes to energy losses, and thus a higher harmonic content results in increased machine losses. Furthermore, the impact of these harmonics is exacerbated by the growing trend of using a reduced number of turns in series per phase. This practice decreases winding inductances, leading to a higher current ripple. Indeed, [2] provided a simplified expression for the maximum peak-to-peak current ripple amplitude ΔI_{pk-pk}, highlighting that it is inversely proportional to the machine inductance and to the switching frequency (1).

$$\Delta I_{pk-pk} \approx \frac{V_{DC} \cdot d}{2\sqrt{3}L \cdot f_{sw}} \propto \frac{1}{L} \tag{1}$$

Where d is the modulation index, L is the machine inductance, V_{DC} is the DC link voltage and f_{sw} is the inverter switching frequency. The industrial trend of increasing the inverter switching frequencies [3] [4] decreases the ΔI_{pk-pk} but pushes the current harmonics at higher frequencies. In addition, the high electrical conductivity of rare-earth magnets aggravates the eddy current PM loss.
Overall, the machine efficiency under PWM supply can significantly differ from the one computed with an ideal sinusoidal supply, especially when dealing with high current ripple drives.

B. Scope of the paper

The proposed efficiency mapping procedure encompasses machine control, FEA and MATLAB data manipulation, as outlined in Fig.1. The outcome is an efficiency map that considers critical and impactful aspects not limited to the PWM supply effect. Indeed, the iron loss model contemplates major and minor hysteresis loops, the flux density DC bias

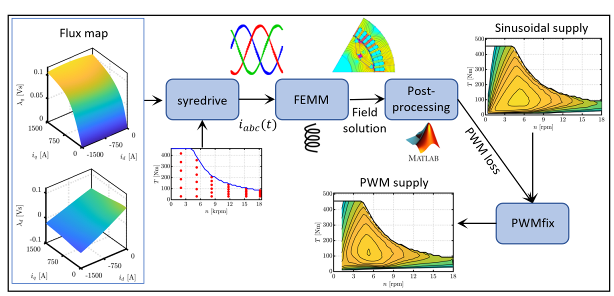

Fig. 1. Flowchart of the efficiency mapping procedure accounting for the PWM supply.

TABLE I
TESLA MODEL 3 3D5 RATINGS [5].

Max current	I_{max}	1414	[Apk]
Max torque	T_{max}	430	[Nm]
Min DC link voltage	$V_{dc,min}$	231	[V]
Nominal DC link voltage	V_{dc}	255	[V]
Base speed	n_{base}	4200	[rpm]
Max speed	n_{max}	18100	[rpm]
Max power	P_{max}	192	[kW]
Switching frequency	f_{sw}	10	[kHz]

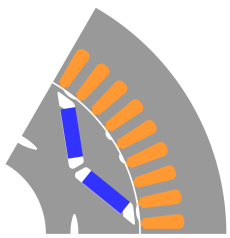

Fig. 2. Radial cross-section of the benchmark resembling the motor mounted on the Tesla Model 3 3D5.

and the mechanical compressive stress. Regarding the magnet loss, the reaction field and 3D effect are considered.

The procedure takes flux maps as inputs, which are utilized as Look-Up Tables (LUTs) within the Simulink dynamic model embedded in SyR-e [6], referred to as "syreDrive" [7]. Its outputs are a set of three-phase non-sinusoidal current waveforms, which are then forwarded to the static FEA model in FEMM [8]. Subsequently, advanced loss models are exploited to compute iron, magnet and copper loss. To optimize computational efficiency, only a limited number of points are simulated with non-sinusoidal current waveforms. The final efficiency map under PWM supply is obtained by interpolating adjustment factors, which represent the ratio between losses under PWM supply and sinusoidal supply. This step, referred to as "PWMfix," enables the derivation of a comprehensive efficiency map under PWM supply by starting with an efficiency map generated under sinusoidal supply and incorporating data from a limited number of points simulated under PWM supply.

To showcase the process, a motor resembling the one mounted on the Tesla Model 3 3D5 is employed. Its rating and radial cross-section are displayed in Tab. I and Fig. 2, respectively.

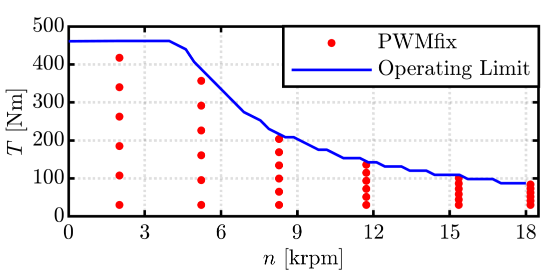

Fig. 3. Operating limits at Θ_{PM}= 80°C and PWMfix points (6x6 grid) for the benchmark.

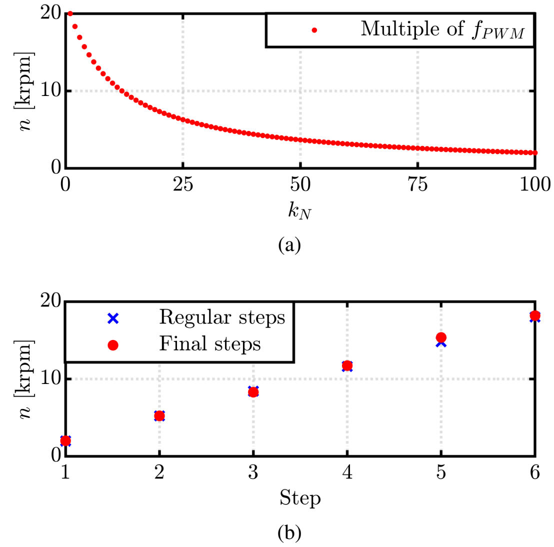

Fig. 4. (a) Rotational speed with a fundamental period integer multiple of the switching period and (b) regular and final speed steps.

II. CIRCUITAL SIMULATION OF THE DRIVE

A. Selection of the PWMfix points on the T-n domain

To initiate the process, the working points for conducting the loss analysis under PWM supply need to be chosen, namely the PWMfix points.

In the context of the torque-speed domain, a reference operating limit at the selected PM temperature is considered, as depicted in Fig. 3. Subsequently, a grid is delineated within this operating limit, with a specific number of points in both the torque and speed directions. For instance, a grid with dimensions of 6x6, as illustrated in Fig. 3, can be utilized.

The selection of speeds is performed in a manner that ensures the simulated electric periods are integer multiples of the switching period. This approach allows for capturing an integer number of switching cycles within each simulation. Mathematically, this requirement is expressed by (2).

$$t_{fund} = \frac{k_N}{f_{sw}} \rightarrow n = k_N \cdot \frac{p}{60\, f_{PWM}} \tag{2}$$

Where k_N is an integer positive number and t_{fund} is the fundamental period. The relationship (2) is plotted in Fig.4a.

The user specifies the desired speed range and the number of steps. Then, the algorithm identifies the nearest speed steps that fulfil the condition in (2). For example, considering a speed range of 2000-18000 rpm with 6 steps, Fig. 4b illustrates the regular steps in blue and the final ones, marked in red, that will be simulated. As mentioned, the red circles correspond to the closest speed values based on Fig. 4a and (2), starting from the regular speed steps.

Once a torque-speed grid is established, the algorithm calculates the losses under PWM supply, as explained in the section III.

B. Circuital model: syredrive

A circuital model of the electric drive is employed to compute the motor currents under PWM supply and field-oriented control. This model is implemented in Simulink and is rooted in the Voltage Behind Reactance (VBR) approach [9] and utilizes flux maps. In Fig. 5, the motor is represented as an RLE load, featuring a three-phase coupled inductor. Controlled voltage generators enforce the back EMF voltage. The coupled inductor takes into account the dq incremental inductances expressed in abc coordinates, which are pre-calculated based on the dq flux maps. The back-EMF voltages are determined by multiplying the dq flux linkage at the relevant operating point by the angular frequency in abc coordinates, utilizing the flux linkage maps once again.

This model is an integral part of the SyR-e tool, named syreDrive [7]. The accuracy of this circuital model has been validated through experimentation, as reported in [10], which involved comparing simulated and measured waveforms under steady-state conditions. It is worth noting that syreDrive is also capable of constructing and running a PLECS model [11], which is equivalent to the Simulink model described here.

After simulating the operating point in the torque-speed plane using syreDrive, the next step involves extracting the appropriate current waveforms from the complete current envelope depicted in Fig. 6a. To obtain current waveforms suitable for FEA simulation, the listed requirements must be fulfilled:

- The extracted waveforms must cover one electric period and be in a steady-state condition.
- The starting point of the waveforms must be coherent with the FEA model, meaning that the rotor's position at the initial moment must coincide with that in the FEA model.

The requirements are satisfied by initially selecting the last two electric periods of the full current, therefore, an electric period is extracted starting from the proper instant (namely, rotor position in Simulink equal to the one on the FEA model). As a result, the current waveforms illustrated in Fig. 6b are obtained and are now ready for use as input in the corresponding FEA model.

Finally, the PWMfix approach is implemented across a 6x6 torque-speed grid, as shown in Fig. 3, encompassing 36

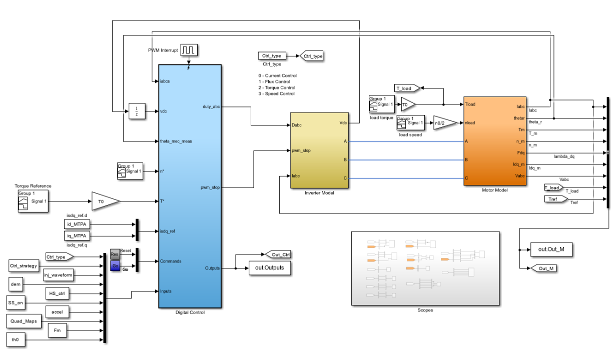

Fig. 5. syreDrive template model in Simulink.

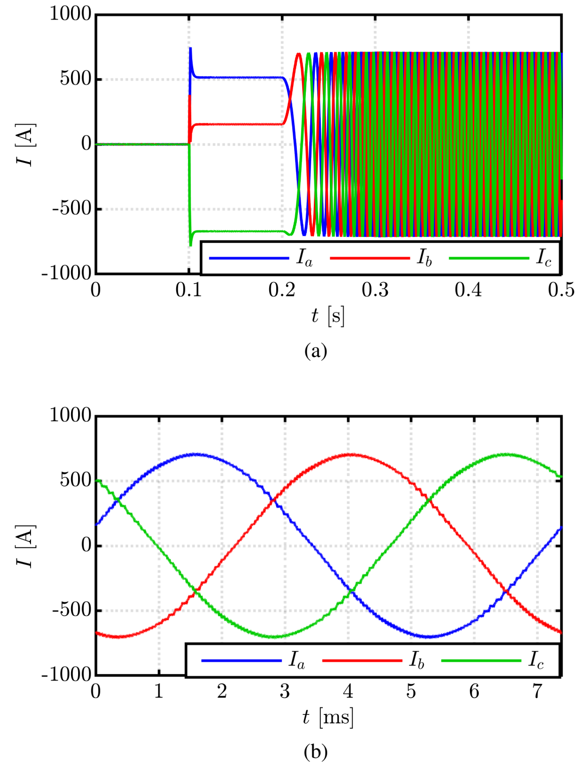

Fig. 6. (a) Full envelope of the current vs time curve from syreDrive and (b) extracted current waveforms for FEA simulations.

distinct operational points. For each of these points, the execution of the syreDrive model leverages parallel computing to obtain the actual non-sinusoidal current waveforms. The discussed step is swift and it covers a minor part of the total computational time. Indeed, to extract the current waveforms in 36 operating points, 10 minutes are requested with the reference working station using an Intel Xeon E5-2690 v4, 14 cores and 32GB.

III. Loss models

A. Iron loss model

The iron loss model is based on the improved Generalized Steinmetz Equation (iGSE) [12] [13] with add-ons to contemplate the DC bias effect [14] and the stator mechanical stress due to shrink-fitting [15]. Below, a brief overview is presented; however, for a more detailed understanding, please consult the provided references.

To showcase the iron loss phenomena in PMSM, Fig. 7 depicts hysteresis loops traced by sinusoidal flux density waveforms with different frequencies, amplitude and DC bias B_{DC}.

Concerning the loss model, the original iGSE [12] is firstly applied via MATLAB scripting to the FEMM field solution to retrieve the iron loss of each mesh element (3).

$$p_{Fe,iGSE} = \frac{1}{T}\int_0^T k_{iGSE}\left|\frac{dB}{dt}\right|^{\alpha}(\Delta B)^{\beta-\alpha}dt \qquad (3)$$

Where ΔB is the peak-to-peak flux density of the considered loop and the k_{iGSE} is retrieved by the Steinmetz coefficient

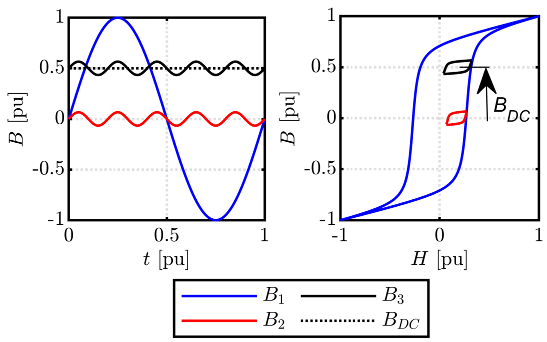

Fig. 7. Flux density waveforms tracing the major (blue) and minor (red and black) hysteresis loops.

as (4), which are calculated by fitting the manufacturer loss curves.

$$k_{iGSE} = \frac{k_{SE}}{(2\pi)^{\alpha-1}\int_0^{2\pi}|\cos\theta|^{\alpha}\,2^{\beta-\alpha}d\theta} \tag{4}$$

Where θ is the angular position in electrical degrees.
Once the iron losses for each mesh element and hysteresis loop are computed according to the original iGSE ($p_{Fe,iGSE}$), adjustments are applied to contemplate the minor loop enlargement due to the flux density DC bias as well as the compressive stress produced by the shrink fitting, as in (5).

$$p_{Fe} = k_{Fe,DC}\cdot k_{Fe,mech}\cdot p_{Fe,iGSE} \tag{5}$$

Where the DC bias factor [14] is computed as:

$$k_{Fe,DC} = 0.65B_{DC}^{2.1} + 1 \tag{6}$$

and the compressive stress factor [15] is calculated as:

$$k_{Fe,mech} = 1 + (C_{h,max}-1)e^{-\frac{B}{B_h}}\cdot(1-e^{-\frac{|\sigma|}{\sigma_h}}) \tag{7}$$

where, the coefficients $C_{h,max}$, B_h and σ_h describe the loss variation with flux density and stress; they were retrieved by experiments on the studied core ($C_{h,max}$ = 4.9, B_h = 0.7 T and σ_h = 100 MPa).

B. Magnet loss model

The static PM losses $P_{PM,stat}$, which neglect reaction field and 3D effects, are retrieved by the FEMM field solution by using the formulation (8).

$$P_{PM,stat} = 2\sigma_m\pi^2\sum_h\int_V\left(f_h\cdot J_{m,h}\right)^2 dV \tag{8}$$

where σ_m is the magnet conductivity, V is the magnet volume, $J_{m,h}$ and f_h are respectively the current density and the frequency at the h-th harmonic. Subsequently, the coefficients $k_{PM,RF}$ and $k_{PM,3D}$ are applied to every loss harmonics, turning the initial formulation of the PM losses (8) into (9).

$$P_{PM} = 2\sigma_m\pi^2\sum_h\Big(k_{PM,RF,h}\cdot k_{PM,3D,h}\cdot\int_V\left(f_h\cdot J_{m,h}\right)^2 dV\Big) \tag{9}$$

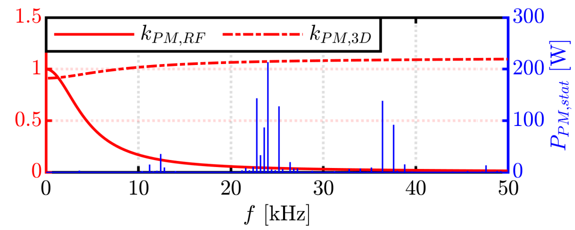

Fig. 8. Magnet loss computation by applying correction factors to the magnetostatic solution.

Details on the coefficients $k_{PM,RF}$ and $k_{PM,3D}$ are provided in [16]. Consequently, given a current density results from a static FEA, every PM loss harmonics is multiplied by its respective coefficients $k_{PM,RF,h}$ and $k_{PM,3D,h}$, as depicted in Fig. 8, to contemplate the reaction field and the 3D effects.

C. Copper loss model

Concerning the copper loss, the pre-calculated AC factor map ($k_{AC} = \frac{R_{AC}}{R_{DC}}$) is exploited. The map, shown in Fig. 9 with reference to the case study, is a function of frequency and copper temperature and it is built with linear time harmonics simulation [13]. Specific simulations are executed on two slot models at different frequencies and copper temperatures to retrieve the AC loss effect along the active length ($k_{AC,act}$,) and on the end-winding ($k_{AC,ew}$).

$$k_{AC,act} = \frac{R_{AC,act}}{R_{DC,act}} \tag{10}$$

$$k_{AC,ew} = \frac{R_{AC,ew}}{R_{DC,ew}} \tag{11}$$

where the subscripts 'act' and 'ew' associated with the resistances correspond to the active length and end-winding values, respectively.
Thus, the AC loss factor k_{AC} is computed by merging both contributions:

$$k_{AC} = k_{AC,act}\cdot\frac{l}{l+l_{ew}} + k_{AC,ew}\cdot\frac{l_{ew}}{l+l_{ew}} \tag{12}$$

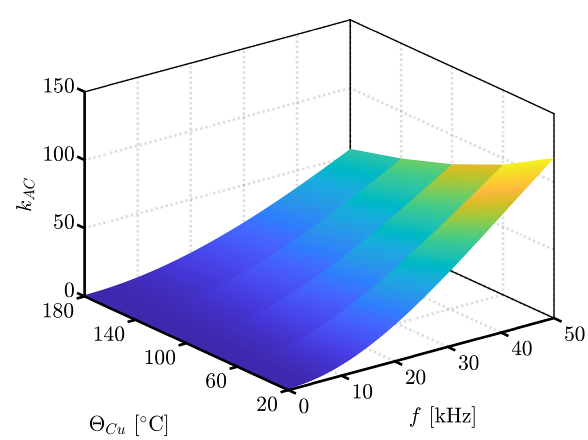

Fig. 9. AC loss factor function the copper temperature and the frequency.

where l and l_{ew} represent the active and end-winding lengths, respectively.

IV. FEA SIMULATIONS AND EFFICIENCY MAPS

A. Iron and magnet loss simulation

The discussed loss models are employed in a FEA simulation executed with the non-sinusoidal current waveforms obtained as in section II-B.

Concerning the FEA setup, the number of simulated rotor positions must be chosen according to the desired number of samples at the target frequency. To do so, a sample current is used with a fundamental current waveform at 100Hz with a peak value of 500Apk, superimposed by a rippling current of 40Apk at 20kHz. It is important to emphasize that, to obtain losses using the proposed model, it is necessary to simulate half of the electric period (by exploiting electric symmetry as in [13]). Thus, FEA simulations are run with different numbers of rotor positions, spanning from 100 to 1000 samples in half electric period, namely 2 to 20 samples in the target period which is 20kHz in this example. Fig. 10 demonstrates that 10 samples at the target period represent an optimal trade-off between accuracy and computational time. Then, in this specific example, 500 rotor angular positions are simulated in half electric to properly capture the loss produced by the 20kHz harmonic.

Therefore, the efficiency mapping algorithm adeptly determines the number of rotor positions for every rotor speed to properly capture the harmonics up to a target value. In particular, aiming to cover twice the switching frequency, the number of rotor positions $N_{rot,step}$ can be conveniently defined as indicated in (13).

$$N_{rot,step} = 10 \cdot \frac{t_{fund}/2}{t_{PWM}/2} = \frac{30}{np} \cdot 10 \cdot (2 f_{sw}) = \frac{600 f_{sw}}{np} \quad (13)$$

where t_{fund} and t_{PWM} are respectively the fundamental electric period and the switching period.

Additionally, this equation emphasizes a crucial point: at lower speeds, the necessary number of rotor positions increases, resulting in a corresponding rise in computational time. Hence,

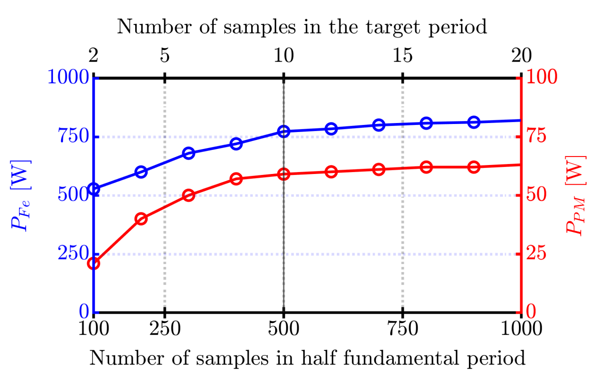

Fig. 10. Iron and magnet loss as function the number of samples in a target period (20kHz) or in half of the fundamental period (100Hz).

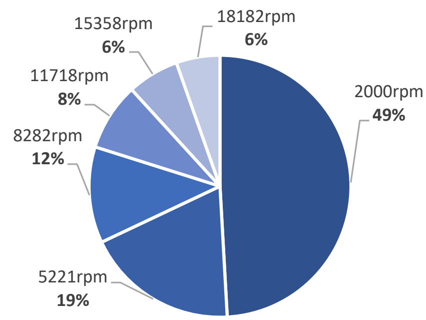

Fig. 11. Breakdown of the FEA computational time for a 6x6 torque-speed grid with reference to the workstation (Intel Xeon E5-2690 v4, 14 cores and 32GB). The total computation time is around 80 minutes.

the choice of the minimum speed selected substantially influences the computational time. To provide an illustrative example, the PWMfix points in Fig. 3 are taken into account, and the corresponding computational times are presented in Fig. 11, categorized by rotational speed. It is worth noting that the minimum speed points account for half of the total computational time.

B. Copper loss computation

The non-sinusoidal current waveforms are decomposed with an FFT and each harmonic (I_h) is associated with a related AC factor ($k_{AC,h}$), as in (14) and as depicted in Fig. 12 for a sample operating point.

$$P_{Cu} = 3\, R_{DC} \cdot \sum_{h=0}^{\infty} k_{AC,h} \cdot I_h^2 \quad (14)$$

This stage does not require additional FEA, since it solely uses the pre-calculated AC loss map (Fig. 9) by exploiting the superposition principle.

C. The PMWfix method and efficiency maps

At this stage, correction factors are computed for every loss component as ratios between loss under PWM supply and sinusoidal supply. Consequently, the correction factors are subjected to linear interpolation and extrapolation across the entire torque-speed domain. Thus, the sinusoidal loss maps are fine-tuned through multiplication with these correction factor maps. Last, the efficiency data is updated according to the

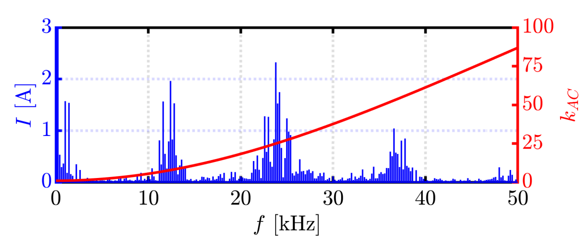

Fig. 12. Copper loss computation by applying the AC loss factor to the current harmonics.

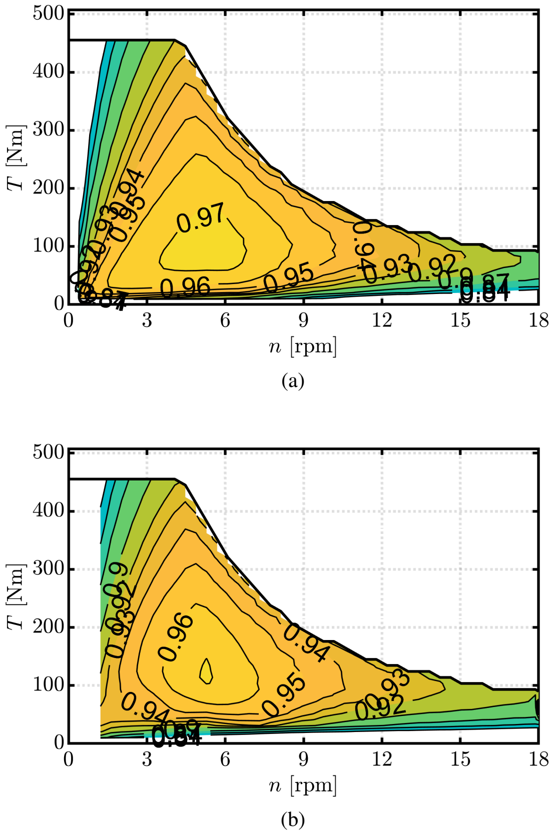

Fig. 13. Efficiency map of the Tesla Model 3 3D5 benchmark under (a) sinusoidal and (b) PWM supplies with Θ_{PM}=80°C and Θ_{Cu}=80°C.

corrected loss map. Fig. 13 reports the efficiency maps under sinusoidal and PWM supply, demonstrating the significant efficiency shrinkage due to the PWM. The impact of the PWM supply on PM loss is evident, resulting in a substantial increase up to 80 times. While this surge may not be pivotal for overall efficiency, it holds paramount significance in characterizing the machine's thermal behaviour. Last, iron losses experienced a notable upswing of up to 2.5 times due to the PWM supply. This escalation significantly affects both efficiency and thermal characteristics. Notably, copper losses witness a restrained increase with PWM supply, but a greater hike is expected with the adoption of hairpin windings.

V. Conclusion

This manuscript presents a novel and agile efficiency mapping procedure for PMSMs, considering the impact of PWM supply. The efficacy of the procedure is exemplified through its application to a traction PMSM, demonstrating its inherent value and effectiveness. Emphasis is placed on the imperative integration of machine control and design, addressing the pressing need for synergy between the two domains. The efficiency computed with PWM supply in around 90 minutes deviates from that calculated under ideal sinusoidal supply, underscoring the influence of PWM on performance metrics. Magnet loss has the most relative increase due to PWM supply, impacting the overall performance continuity. While iron losses experience a relatively modest percentage increase, but a significant absolute hike that influences the overall efficiency results.

Acknowledgment

The research has been conducted with the support of Power Electronics Innovation Center (PEIC) of Politecnico di Torino.

References

[1] J. Kolar, H. Ertl, and F. Zach, "Influence of the modulation method on the conduction and switching losses of a PWM converter system," *IEEE Transactions on Industry Applications*, vol. 27, no. 6, pp. 1063–1075, Nov. 1991.

[2] G. Grandi and J. Loncarski, "Evaluation of current ripple amplitude in three-phase PWM voltage source inverters," in *2013 International Conference-Workshop Compatibility And Power Electronics*, Jun. 2013, pp. 156–161, iSSN: 2166-9546.

[3] F. Stella, E. Vico, D. Cittanti, C. Liu, J. Shen, and R. Bojoi, "Design and Testing of an Automotive Compliant 800V 550 kVA SiC Traction Inverter with Full-Ceramic DC-Link and EMI Filter," in *2022 IEEE Energy Conversion Congress and Exposition (ECCE)*. Detroit, MI, USA: IEEE, Oct. 2022, pp. 1–8.

[4] D. Cittanti, F. Stella, E. Vico, C. Liu, J. Shen, G. Xiu, and R. Bojoi, "Analysis, Design, and Experimental Assessment of a High Power Density Ceramic DC-Link Capacitor for a 800 V 550 kVA Electric Vehicle Drive Inverter," *IEEE Transactions on Industry Applications*, vol. 59, no. 6, pp. 7078–7091, Nov. 2023.

[5] MotorXP-PM, "Performance Analysis of the Tesla Model 3 Electric Motor using MotorXP-PM," Tech. Rep., Jun. 2020. [Online]. Available: https://motorxp.com/wp-content/uploads/mxp_analysis_TeslaModel3.pdf

[6] G. Pellegrino and F. Cupertino, "SyR-e." [Online]. Available: https://github.com/SyR-e

[7] A. Varatharajan, D. Brunelli, S. Ferrari, P. Pescetto, and G. Pellegrino, "syreDrive: Automated Sensorless Control Code Generation for Synchronous Reluctance Motor Drives," in *2021 IEEE Workshop on Electrical Machines Design, Control and Diagnosis (WEMDCD)*. Modena, Italy: IEEE, Apr. 2021, pp. 192–197.

[8] D. Meeker, "FEMM: Finite Element Method Magnetics." [Online]. Available: www.femm.info

[9] C. Rollbuhler, S. Peukert, D. Fritz, J.-F. Heyd, J. Kolb, and M. Doppelbauer, "Investigations on the Experimental Identification of AC-Copper Losses in Permanent Magnet Synchronous Machines using a Motor Sub-Assembly," in *IECON 2019 - 45th Annual Conference of the IEEE Industrial Electronics Society*. Lisbon, Portugal: IEEE, Oct. 2019, pp. 1150–1156. [Online]. Available: https://ieeexplore.ieee.org/document/8926835/

[10] A. Bojoi, "Advanced Dynamic Model of E-motor for Control Rapid Prototyping," laurea, Politecnico di Torino, Mar. 2022. [Online]. Available: https://webthesis.biblio.polito.it/22088/

[11] "Electrical Engineering Software | Plexim." [Online]. Available: https://www.plexim.com/

[12] K. Venkatachalam, C. Sullivan, T. Abdallah, and H. Tacca, "Accurate prediction of ferrite core loss with nonsinusoidal waveforms using only Steinmetz parameters," in *2002 IEEE Workshop on Computers in Power Electronics, 2002. Proceedings.*, Jun. 2002, pp. 36–41, iSSN: 1093-5142.

[13] S. Ferrari, P. Ragazzo, G. Dilevrano, and G. Pellegrino, "Flux and Loss Map Based Evaluation of the Efficiency Map of Synchronous Machines," *IEEE Transactions on Industry Applications*, vol. 59, no. 2, pp. 1500–1509, Mar. 2023.

[14] C. Simao, N. Sadowski, N. J. Batistela, and J. P. A. Bastos, "Evaluation of Hysteresis Losses in Iron Sheets Under DC-biased Inductions," *IEEE Transactions on Magnetics*, vol. 45, no. 3, pp. 1158–1161, Mar. 2009.

[15] K. Yamazaki and H. Takeuchi, "Impact of Mechanical Stress on Characteristics of Interior Permanent Magnet Synchronous Motors," *IEEE Transactions on Industry Applications*, vol. 53, no. 2, pp. 963–970, Mar. 2017.

[16] M. Hullmann and B. Ponick, "General Analytical Description of the Effects of Segmentation on Eddy Current Losses in Rectangular Magnets," in *2022 International Conference on Electrical Machines (ICEM)*. Valencia, Spain: IEEE, Sep. 2022, pp. 1757–1762.